J. Fluid Mech. (2011), *vol.* 678, *pp.* 5–13.
doi:10.1017/S002211201100005X

Tethered fleximags as artificial cilia

AVIN BABATAHERI[1], MARCUS ROPER[2,3], MARC FERMIGIER[1]† AND OLIVIA DU ROURE[1]

[1]Physique et Mécanique des Milieux Hétérogenes, UMR 7636 CNRS/ESPCI ParisTech, Université Pierre et Marie Curie, Universite Paris Diderot, 10, rue Vauquelin, 75005 Paris, France

[2]Department of Mathematics and Lawrence Berkeley National Laboratory, University of California, Berkeley, CA 94720, USA

[3]Mathematics Institute, University of Warwick, Coventry CV4 7AL, UK

(Received 27 October 2010; revised 27 October 2010; accepted 23 December 2010; first published online 15 March 2011)

Flexible superparamagnetic filaments ('fleximags') are very slender elastic filaments, which can be driven by distributed magnetic torques to mimic closely the behaviour of biological flagella. Previously, fleximags have been used as a basis for artificial micro-swimmers capable of transporting small cargos Dreyfus *et al.* (*Nature*, vol. 437, 2005, p. 862). Here, we demonstrate how these filaments can be anchored to a wall to make carpets of artificial micro-magnetic cilia with tunable densities. We analyse the dynamics of an artificial cilium under both planar and three-dimensional beating patterns. We show that the dynamics are controlled by a single characteristic length scale varying with the inverse square root of the driving frequency, providing a mechanism to break the fore and aft symmetry and to generate net fluxes and forces. However, we show that an effective geometrical reciprocity in the filament dynamics creates intrinsic limitations upon the ability of the artificial flagellum to pump fluid when driven in two dimensions.

Key words: Low-Reynolds-number flows, MEMS/NEMS, swimming/flying

1. Introduction

Assemblies of cilia and isolated flagella are used by microorganisms to propel themselves in liquids, and by multi-celled organisms for internal transport of fluids or materials, including the clearance of mucus from airways and the movement of ova along oviducts (Brennen & Winet 1977). Nodal cilia also play a crucial role in determining the bilateral asymmetry of developing embryos (Nonaka *et al.* 1998; Cartwright, Piro & Tuval 2004; Buceta *et al.* 2005). The structure of cilia is highly conserved across many species, including mammals and ciliated protists. Cilia are very flexible, possess a very large aspect ratio and their three-dimensional motion is due to distributed bending torques generated by internal molecular motors (Camalet, Jülicher & Prost 1999). The desire to understand in detail the fluid dynamics of assemblies of cilia and to create pumps and mixers for microfluidic devices has prompted the fabrication of artificial cilia-like structures, such as carpets of PDMS pillars loaded with maghemite nanocolloids (Evans *et al.* 2007). Recent studies have shown the feasibility of fluid transport by rigid superparamagnetic rods if tethered to

† Email address for correspondence: marc.fermigier@espci.fr

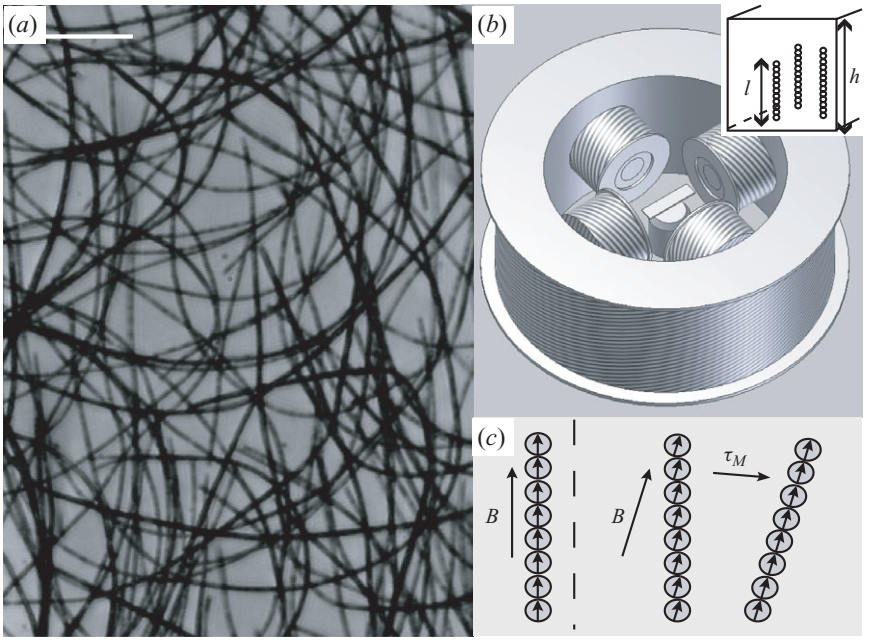

FIGURE 1. (*a*) Fleximags. Scale bar: 50 μm. (*b*) Coil set-up around the sample and microscope objective. Inset: Magnetic filaments within a rectangular capillary tube. (*c*) Actuation mechanism.

a substrate (Shields *et al.* 2010; Vilfan *et al.* 2010) or allowed to walk, fragment and reassemble (Sing *et al.* 2010).

Here, we use the ability of superparamagnetic colloids to self-assemble into long chains, which can be permanently linked by adsorbed polymer to create micromagnetic filaments (fleximags) (Dreyfus *et al.* 2005; Goubault *et al.* 2005) and graft these filaments to chemically treated surfaces to make microscopic flexible artificial cilia (figure 1). Our artificial cilia share key common features with real cilia, namely a very large aspect ratio, high flexibility and the ability to follow complex trajectories in three dimensions without being subjected to a net external force.

The key feature in our system is the existence of a characteristic mobile length resulting from the balance between magnetic driving and viscous resistive torques which decreases as the inverse square root of the driving frequency. This frequency dependence provides the basis for breaking the fore and aft symmetry of the filament motion to generate a net average flux of fluid along the substrate. However, we show that because of a hidden geometric reciprocity of the filament motion, the net force remains small, directly confirming and explaining the very low pumping efficiencies observed in previous simulation-based studies (Kim & Netz 2006; Downton & Stark 2009).

2. Experiments

We fabricate the tethered cilia *in situ* from superparamagnetic colloidal particles (radius $a = 350$ nm, magnetic susceptibility $\chi \approx 1$) which are linked together by polyacrylic acid (PAA, MW = 250 000) (Goubault *et al.* 2003). A suspension of magnetic colloids (volume fraction $\phi \approx 0.1\,\%$), nonyl phenol ethoxylate (0.1 % wt/wt, surfactant, NP10 Sigma) and PAA (0.1 % wt/wt) is injected in a rectangular capillary tube held at the centre of a system of magnetic coils (figure 1*b*). We create functional carpets

of cilia by coating the walls of the capillary tube with L-polylysine (Sigma, incubation one night at 0.01 % wt/wt) to promote the adhesion of the magnetic filaments. By aging the wall-coating, we can control the density of cilia. The suspension is held in a constant vertical magnetic field ($B \approx 24$ mT) for 30 min. During this incubation time, long filaments, essentially one particle in diameter, are formed. Then, the suspension is washed away by clear fluid and only a few filaments per mm^2 remain on the tube wall. Their length, L, can be varied between 50 and 300 μm. The bending coefficient of the filaments κ, measured as described before (Goubault *et al.* 2003), is $\kappa \approx 8 \times 10^{-26}$ J m.

A time-varying magnetic field, created by the magnetic coils, causes the artificial cilia to flex and bend. Just as for a real flagellum, this magnetic actuation produces no net force upon each artificial cilium, but produces internal torques along the length of the filament. The dipole moment $\boldsymbol{m}$ of a single superparamagnetic colloid is parallel to the applied field $\boldsymbol{B}$. If, however, the local orientation of the filament is not parallel to the field, then, because of the dipole–dipole interaction between colloids, a net torque is developed which tends to realign the filament (figure 1*c*). This local driving magnetic torque is given by:

$$\tau_M = \frac{\pi a^2 B^2}{6\mu_0} \chi_e^2 \sin(2\alpha), \tag{2.1}$$

where α is the angle between the field and the local filament axis, and χ_e denotes effective susceptibility (Roper *et al.* 2006).

The three field components are generated by independent sets of coils driven by bipolar amplifiers ($|B| = 4$–10 mT). We investigated planar periodic motions and three-dimensional (3D)-rotations. For planar oscillations, we visualize the entire filament by tilting the plane of oscillation by an angle 25° with respect to the optical axis. The z and y field components are constant in time, while the x component oscillates (figure 2*b*). To generate a symmetric motion, we impose $B_x(t) = B_0 \cos(\omega t)$, with a frequency ranging from 0.1 to 5 Hz. To induce a precession of the filament, the field rotates on a cone around the z axis: B_z is constant while B_x and B_y oscillate in phase quadrature (figure 2*d*). The cone angle θ ranges from 10° to 40°.

For both planar and 3D actuation, the amplitude of filament motion decreases as we increase the beating frequency, ω (figure 2) (movies are available as supplementary material at journals.cambridge.org/flm). To reconstruct the shape of the beating filament, we image the filament trajectory at six different z positions. Projecting all images, for a given time, onto a single plane gives a focused image all along the filament. This resulting image is processed to obtain a smooth and differentiable shape. The dependence of amplitude upon frequency can be understood from the torque balance on a flexible magnetic filament of length ℓ driven at an angular velocity ω: here, the driving torque $\Gamma_m = (\ell/2a)\tau_M$, and is balanced both by a viscous torque, Γ_v, due to the friction of the surrounding fluid and a bending torque, Γ_b, due to the elasticity of the linker between particles in the filament. For a slender rod, $\Gamma_v \sim \zeta_\perp \omega \ell^3$, where $\zeta_\perp$ is the drag per unit length of filament, while $\Gamma_b \sim \kappa/\ell$. Thus, viscous torques can balance the magnetic torque on a magnetoviscous length scale: $\ell_{mv}/L \sim Ma^{-1/2}$ and bending torques can balance the magnetic torque on a magnetoelastic length scale: $\ell_{mb}/L \sim Mn^{-1/2}$, where Ma and Mn are the *Mason* and *magnetoelastic* numbers introduced by Melle *et al.* (2003), Cebers (2003) and Roper *et al.* (2006):

$$Ma = \frac{\zeta_\perp \omega L^2 \mu_0}{a^2 B^2 \chi_e^2}, \qquad Mn = \frac{a^2 \chi_e^2 B^2 L^2}{\mu_0 \kappa}. \tag{2.2}$$

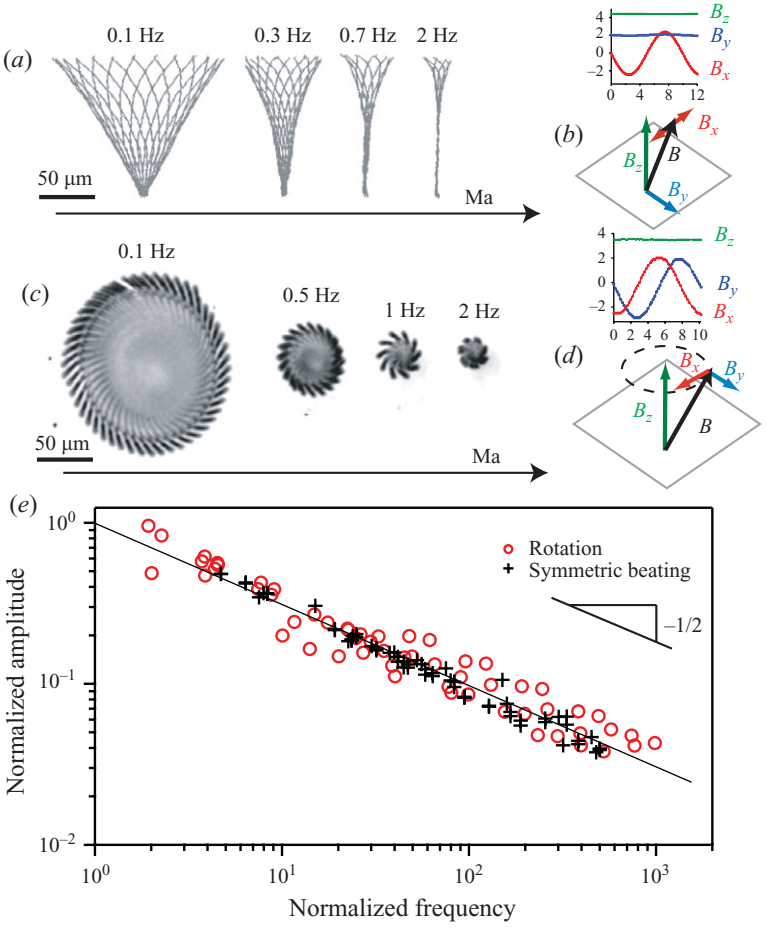

FIGURE 2. (Colour online) Tip amplitude and mobilized length decrease as the driving frequency is increased. (*a*) Shapes of filaments, reconstructed from top view, for planar oscillations at four different frequencies. (*b*) Driving magnetic fields for planar motion. (*c*) Excursion of filament tip (top view) for 3D rotations. (*d*) Magnetic fields for 3D rotation. (*e*) Relative filament tip displacement as a function of Mason number for planar beating (○, $L = 160$, 180 and 220 μm) and rotation (+, $L = 150 \rightarrow 300\,\mu\text{m}$ and θ from 10° to 40°).

In our experiments, $B \sim 10\,\text{mT}$ and $L \sim 100\,\mu\text{m}$, so $Mn \sim 10^5$ is much larger than $Ma \sim 1$–1000, so the dominant resistance to the magnetic torque comes from viscous drag and the intrinsic elasticity of the filaments can be neglected.

Although filament bending stiffness can be neglected, the interplay of dipole interactions, which tend to straighten the filament, and viscous loading, endows the filament with a dynamically varying characteristic bending scale ℓ_{mv}, effectively making it rigid to slow motions and flexible to fast motions. Because the free end of the filament must track the direction of the time-varying applied field, we expect, from the above scalings, that the amplitude of the free end motion $A \sim \ell_{mv} \propto Ma^{-1/2}L$. For planar filament beating, A/L follows exactly the expected scaling law (figure 2*e*). The same dependence is seen for the radius R of the circle traced out by the tip of a rotating filament when the radius and filament length are correctly scaled. In this case, the filament is bent so that most of the filament is aligned with the steady (vertical) part of the field, while a short mobile section of length ℓ near the

free end traces out a circle. The azimuthal speed of a point on the mobile section depends on its distance from the vertical axis, giving rise to a total viscous torque $\Gamma_v \sim \zeta_\perp \omega \ell^3 \sin\theta$ so that the mobile length of filament $\ell \sim (Ma \sin\theta)^{-1/2} L$. The radius of rotation, R, is the projection of this mobile length onto the horizontal plane, so $R \sim \ell \sin\theta \sim (Ma \sin\theta)^{-1/2} \times L \sin\theta$.

3. Numerical simulations

A mathematical model quantitatively predicts the fleximag shape and the fluxes that it generates, and allows us to explore a wide parameter space of possible field configurations and filament lengths (Cebers 2003; Roper *et al.* 2006; Keaveny & Maxey 2008; Gauger, Downton & Stark 2009). In the continuum limit, the fleximag is considered as an inextensible filament with centreline $\boldsymbol{r}(s,t)$ varying with time, t, and the distance along the filament, s (Cebers 2003; Roper *et al.* 2006). The local filament velocity is proportional to the net force: $\partial \boldsymbol{r}/\partial t = \boldsymbol{M} \cdot \partial \boldsymbol{f}/\partial \boldsymbol{s}$, where $\boldsymbol{f}$ is the stress resultant across a slice of filament, and the mobility tensor $\boldsymbol{M}$ includes the approximate enhancement in drag due to the proximity of the wall, represented by coefficients $k_{x,z}$:

$$\boldsymbol{M} = \frac{1}{\zeta_\parallel}\boldsymbol{ss} + \frac{1}{\zeta_\perp}(1 - \boldsymbol{ss}) - \frac{k_x}{z+\epsilon}(\boldsymbol{e}_x\boldsymbol{e}_x + \boldsymbol{e}_y\boldsymbol{e}_y) - \frac{k_z}{z+\epsilon}\boldsymbol{e}_z\boldsymbol{e}_z. \tag{3.1}$$

At the same order of error as already made in the resistive force theory, we may choose $2k_x = k_z = L/8\pi\eta$, incorporating only the wall-induced backflow caused by a single Stokeslet at each reference location. A small displacement ϵ is added to keep the mobility tensor positive definite down to $z = 0$. Our simulations are insensitive to the precise form of the regularization, most likely because the filament is held stationary at the wall. We obtain an equation for the filament dynamics by resolving the stress resultant into a tensile force $\Lambda \boldsymbol{s}$, and a normal force, which can be related to the magnetic field by torque balance. In dimensionless variables (scaling s by L, t by $1/\omega$, Λ by $a^2 B_z^2 \chi_e^2/\mu_0$, $\boldsymbol{M}$ by $\zeta_\perp$ and $\boldsymbol{B}$ by B_z), these manipulations give:

$$\frac{\partial \boldsymbol{r}}{\partial t} = \frac{1}{6Ma}\boldsymbol{M} \cdot \frac{\partial}{\partial s}\left[-(\boldsymbol{B}\cdot\boldsymbol{s})(\boldsymbol{B} - (\boldsymbol{B}\cdot\boldsymbol{s})\boldsymbol{s}) + \Lambda \boldsymbol{s}\right] \tag{3.2}$$

with the tension, Λ, given implicitly by the inextensibility condition $|\partial \boldsymbol{r}/\partial \boldsymbol{s}| = 1$. We discretize this pair of partial differential equations using second-order centred differences for the spatial derivatives, and integrate in time using the Matlab differentio-algebraic equation solver ode15s. The computed shapes agree well with experimental observations, showing that the level of approximation used is completely adequate to describe the dynamics (figure 3).

4. Induced fluxes

To generate a flux of fluid using an artificial cilium, we manipulate the frequency of actuation, and thereby the mobile length of the artificial cilium, within a single stroke. Specifically, we divide the actuation cycle into two parts: a fast right-to-left stroke, $B_x(t) \propto \cos(\omega_f t)$ followed by a slow left-to-right stroke, $B_x(t) \propto \cos(\omega_s t)$; in our experiments, $\omega_f/\omega_s = 10$. Filament shapes for this asymmetric actuation are shown in figures 3(*c*), 3(*d*) and 4(*a*).

Because of the dependence of the mobile length on the actuation frequency, this asymmetric actuation should produce a net rightward flux of fluid. We

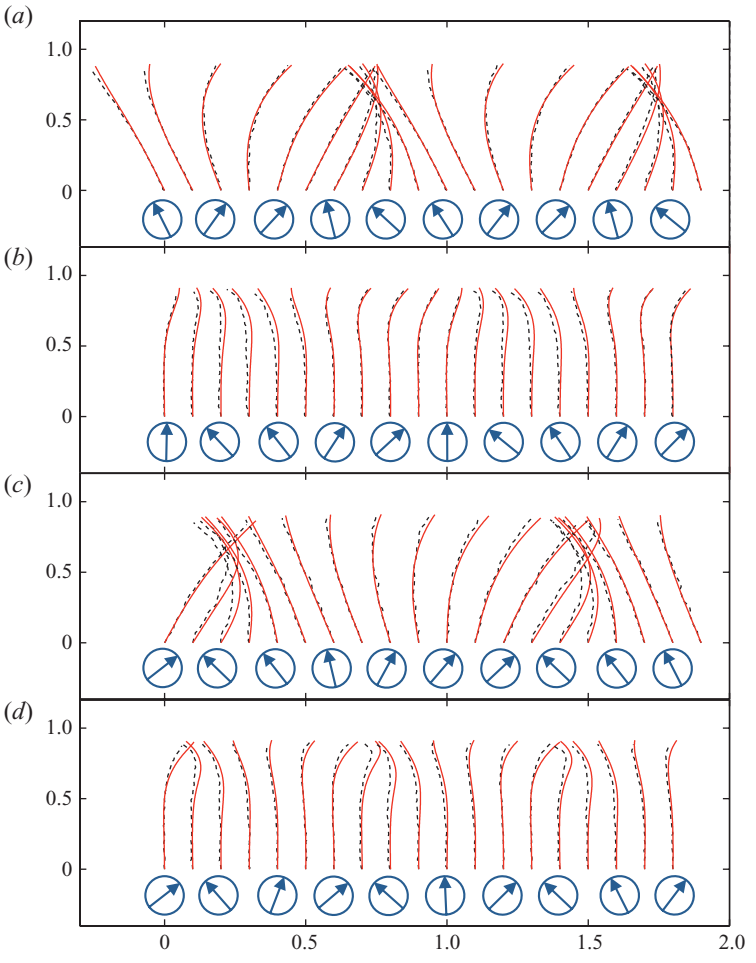

FIGURE 3. (Colour online) Experimental filament shapes (dashed lines) accord very closely with the predictions of a continuum model (solid lines) at (a, c) low (0.1 Hz, $Ma \approx 18$) and (b, d) high (1.0 Hz, $Ma \approx 180$) frequencies; (a) and (b) show symmetric actuation while (c) and (d) show asymmetric actuation. Circled arrows: orientation of the instantaneous magnetic field.

expected that during the fast leftward part of the motion, the mobile length of filament exerts a force $F_f \sim \zeta_\perp \omega_f \ell_{mv}(\omega_f)^2$ upon the fluid, creating a total leftward flow of fluid $\mathscr{F}_f \sim F_f L/\eta\omega_f$ over the fast half-stroke. On applying the same scalings to the slow half-stroke, we predicted net rightward transport, because $|\mathscr{F}_s|/|\mathscr{F}_f| \sim \ell_{mv}(\omega_s)^2/\ell_{mv}(\omega_f)^2 \gg 1$.

In fact, and in confirmation of previous numerical simulations (Kim & Netz 2006; Downton & Stark 2009), in our experiments the total transport over a stroke $|\mathscr{F}_f - \mathscr{F}_s|$ is at least two orders of magnitude smaller than the total unsigned transport $|\mathscr{F}_f + \mathscr{F}_s|$ (figure 4c). Previously, Downton & Stark (2009) attributed this cancellation to the over-damping of the driven filament: at the beginning of the slow rightward half-stroke, the tip of the filament continues to move leftward (illustrated by open circles in figure 4a). Indeed, the persistence of the leftward fast stroke into the rightward part of the motion evens out some of the stroke asymmetry. However, the filament shapes

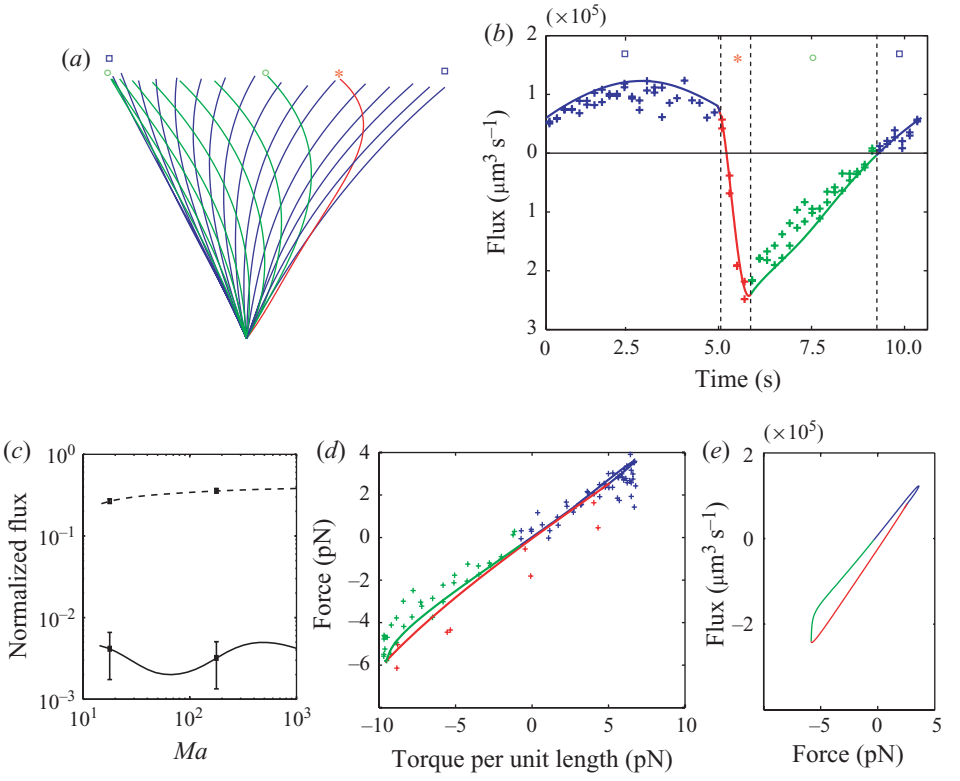

FIGURE 4. The pumping efficiency of planar beating is very low. (*a*) Filament shapes during asymmetric beating: fast-leftward stroke (red, star), slow-rightward stroke (green, open circles, and blue, open squares). (*b*) Instantaneous fluxes generated by a single filament, computed from the experimental (crosses) and simulated (solid line) filament shapes, as a function of time. Asymmetry of filament shapes leads to different flux rates during leftward and rightward strokes. Here colour coding of stroke phases follows (*a*). (*c*) Average dimensionless horizontal flux as a function of frequency for asymmetric actuation, including simulations (curves) and experimental data (points). The solid curve and solid points give the average fluid flux $|\mathscr{F}_f - \mathscr{F}_s|/T$ and the dashed curve and hollow points give the averaged unsigned flux $|\mathscr{F}_f + \mathscr{F}_s|/T$. Fluxes are scaled by $\tau_m L/\zeta_\perp \sim (a^2 B_z^2 \chi_e^2 L/6\mu_0 \pi \zeta_\perp)$. (*d*) Total horizontal force is related in a direct one-to-one manner to the basal torque, so filament dynamics have a single degree of freedom. (*e*) Force and flux are not proportional because of the designed stroke asymmetry.

during leftward and rightward motions are clearly different (figure 4*a*). In addition, the fluxes computed from the experimental or simulated filament shapes using the mobility tensor $\boldsymbol{M}$ vary differently during the fast and slow motions (figure 4*b*). So, the remarkably exact cancellation of leftward and rightward fluxes suggests a deeper underlying symmetry.

We plotted the total force exerted by the filament on the fluid against the magnetic torque at the base of the filament, both inferred from the measured filament shapes. We found that the total force exerted by the filament depends directly in a one-to-one and almost linear fashion on the basal torque (figure 4*d*) so that this particular system has only one effective dynamical degree of freedom. Because the basal torque has zero mean value over an entire stroke, the net force over a complete forcing cycle must be zero. This slaving is a remarkable feature of how the micro-magnetic filament

organizes its shape in motion – neither the flux nor the basal torque themselves are time-reversible (figure 4*b*), and the force is not simply related either to the filament basal angle or to the angle of the magnetic field individually.

Although the net force exerted by the filament is almost zero over a complete cycle of the applied field, the designed asymmetry in filament motion leads to change in the effective height of application of the force during the stroke cycle: $\eta\mathscr{F}/F$. Thus, although the net force is almost exactly reversible, the instantaneous flux is not directly proportional to the force (figure 4*e*) creating small difference in fluxes during leftward and rightward strokes. Nonetheless, the effective reciprocity of motion makes the pumping efficiency very small.

5. Conclusion

Our method for tethering flexible magnetic filaments to rigid surfaces allows the construction of micrometer-scale physical analogues of cilia. We observed large differences in the dynamics of filaments driven at high or low frequencies, but a planar asymmetric actuation, which includes fast and slow half-strokes, produces small net fluxes. We relate this to the direct dependence of the force applied by the filament upon a single dynamical variable, creating a hidden reciprocity in the filament motion. The need to overcome this reciprocity provides a common basis for understanding the efficiency gains associated with two recently proposed modifications of the filament, namely the inclusion of elastic defections along the length of the filament, and actuation of the micro-magnetic filament in two independent directions (Downton & Stark 2009; Gauger *et al.* 2009). Alternatively, we can contemplate maximizing the anisotropic effect of motions close to and far from the wall to turn a reciprocal force into a non-reciprocal flux. While Shields *et al.* (2010) have shown the ability of rather rigid magnetic microrods, actuated on inclined cones, to generate significant fluxes, more flexible cilia allow the realization of more complex and biologically-faithful dynamical behaviours (Coq *et al.* 2010).

We thank P. Jenffer for technical support. M.R. is supported by a fellowship from the Miller Institute for Basic Research in Sciences. This work is supported by the Ile de France region under the SESAME program. Supplementary movies are available at journals.cambridge.org/flm.

REFERENCES

Brennen, C. & Winet, H. 1977 Fluid mechanics of propulsion by cilia and flagella. *Annu. Rev. Fluid Mech.* **9**, 339–398.

Buceta, J., Ibanes, M., Rasskin-Gutman, D., Okada, Y., Hirokawa, N. & Izpisua-Belmonte, J. C. 2005 Nodal cilia dynamics and the specification of the left/right axis in early vertebrate embryo development. *Biophys. J.* **89** (4), 2199–2209.

Camalet, S., Jülicher, F. & Prost, J. 1999 Self-organized beating and swimming of internally driven filaments. *Phys. Rev. Lett.* **82** (7), 1590–1593.

Cartwright, J. H. E., Piro, O. & Tuval, I. 2004 Fluid-dynamical basis of the embryonic development of left-right asymmetry in vertebrates. *Proc. Natl Acad. Sci. USA* **101**, 7234–7239.

Cebers, A. 2003 Dynamics of a chain of magnetic particles connected with elastic linkers. *J. Phys.: Condens. Matter* **15**, S1335–S1344.

Coq, N., Ngo, S., du Roure, O., Fermigier, M. & Bartolo, D. 2010 Three-dimensional beating of magnetic microrods. *Phys. Rev.* E **82**, 041503.

Downton, M. & Stark, H. 2009 Beating kinematics of magnetically actuated cilia. *Eur. Phys. Lett.* **85**, 44002.

Dreyfus, R., Baudry, J., Roper, M. L., Fermigier, M., Stone, H. A. & Bibette, J. 2005 Microscopic artificial swimmers. *Nature* **437** (7060), 862–865.

Evans, B. A., Shields, A. R., Carroll, R. L., Washburn, S., Falvo, M. R. & Superfine, R. 2007 Magnetically actuated nanorod arrays as biomimetic cilia. *Nano Lett.* **7** (5), 1428–1434.

Gauger, E. M., Downton, M. T. & Stark, H. 2009 Fluid transport at low Reynolds number with magnetically actuated artificial cilia. *Eur. Phys. J.* E **28** (2), 231–242.

Goubault, C., Jop, P., Fermigier, M., Baudry, J., Bertrand, E. & Bibette, J. 2003 Flexible magnetic filaments as micromechanical sensors. *Phys. Rev. Lett.* **91**, 260802.

Goubault, C., Leal-Calderon, F., Viovy, J. L. & Bibette, J. 2005 Self-assembled magnetic nanowires made irreversible by polymer bridging. *Langmuir* **21** (9), 3725–3729.

Keaveny, E. & Maxey, M. 2008 Spiral swimming of an artificial micro-swimmer. *J. Fluid Mech.* **593**, 293–319.

Kim, Y. & Netz, R. 2006 Pumping fluids with periodically beating grafted elastic filaments. *Phys. Rev. Lett.* **96**, 158101.

Melle, S., Calderón, O. G., Rubio, M. A. & Fuller, G. G. 2003 Microstructure evolution in magnetorheological suspensions governed by mason number. *Phys. Rev.* E **68**, 041503.

Nonaka, S., Tanaka, Y., Okada, Y., Takeda, S., Harada, A., Kanai, Y., Kido, M. & Hirokawa, N. 1998 Randomization of left–right asymmetry due to loss of nodal cilia generating leftward flow of extraembryonic fluid in mice lacking kif3b motor protein. *Cell* **95** (6), 829–837.

Roper, M., Dreyfus, R., Baudry, J., Fermigier, M., Bibette, J. & Stone, H. A. 2006 On the dynamics of magnetically driven elastic filaments. *J. Fluid Mech.* **554**, 167–190.

Shields, A. R., Fiser, B. L., Evans, B. A., Falvo, M. R., Washburn, S. & Superfine, R. 2010 Biomimetic cilia arrays generate simultaneous pumping and mixing regimes. *Proc. Natl Acad. Sci.* **107** (36), 15670–15675.

Sing, C. E., Schmid, L., Schneider, M. F., Franke, T. & Alexander-Katz, A. 2010 Controlled surface-induced flows from the motion of self-assembled colloidal walkers. *Proc. Natl Acad. Sci. USA* **107**, 535–540.

Vilfan, M., Potočnik, A., Kavčič, B., Osterman, N., Poberaj, I., Vilfan, A. & Babič, D. 2010 Self-assembled artificial cilia. *Proc. Natl Acad. Sci.* **107**, 535–540.